Multicomponent Distributed Acoustic Sensing

Ivan Lim Chen Ning & Paul Sava, Center for Wave Phenomena, Colorado School of Mines

SUMMARY

Distributed Acoustic Sensing (DAS) data in boreholes are not commonly used for reservoir characterization because multicomponent data are needed to quantify different wave modes. We propose two approaches to obtain multicomponent DAS data by using either multiple parallel optical fibers or a helical optical fiber. The multiple parallel optical fibers use the shape sensing method which is based on measurements of axial strain gradient to obtain the curvature of the cable and then reconstruct the components of the displacement field. However, simply using curvature measurements does not provide sufficient information to reconstruct the displacements for different wave modes. The helical optical fiber uses the characteristics of the helix shape to obtain angle dependent strain measurements, which provides sufficient information to reconstruct the strain tensor of the surrounding field.

INTRODUCTION

Distributed Acoustic Sensing (DAS) is rapidly gaining popularity in the oil and gas industry especially for Vertical Seismic Profile (VSP) imaging and for reservoir monitoring (Mestayer et al., 2011; Cox et al., 2012; Mateeva et al., 2012, 2013; Daley et al., 2013; Madsen et al., 2013). The advantages of DAS for borehole applications in terms of costs, the deployment mechanism, and spatial resolution make its usage attractive over conventional geophone acquisition (Lumens et al., 2013; Mateeva et al., 2013).

Lumens (2014) indicates that the DAS system is more sensitive in the axial direction compared to the radial direction, thus reducing the DAS measurable data to the axial strain which can be acquired with acceptable signal-to-noise ratio. Published work does not detail mechanisms for extracting multicomponent data from the axial strain measurement using DAS. To acquire multicomponent data, alternative measuring devices such as geophones are deployed, which are costly and do not provide the dense spatial sampling of DAS. In this paper, we investigate possibilities to use different optical fiber configurations to obtain multicomponent information from DAS data.

Our first approach is to use optical fiber as a shape sensing tool. The relationship between bending and the difference in strain between two Fiber Bragg Gratings (FBG) has been discussed by Gander et al. (2000) as a curvature sensor. Flockhart et al. (2003) and Fender et al. (2006) demonstrate positive experimental results for using this theory as a curvature sensor for structural monitoring. However, their discussion is limited to using the optical fiber as a shape monitoring tool. We exploit shape sensing capabilities to obtain data components that cannot be measured using the axial strain along a single fiber.

Our second approach is to use a helical-shaped optical fiber. Using the characteristics of the helix and axial strain measurement of the optical fiber, we can calculate the entire strain tensor at every measuring location under the assumption that the seismic wavelength is much longer than the helix period. We show the theoretical relationships between the measured axial strain in the optical fiber and the full strain tensor in the surrounding area, and demonstrate the applicability of this strategy using a synthetic example.

MULTIPLE PARALLEL OPTICAL FIBERS

The axial strain measurement by the optical fiber is a projection of the strain tensor from the surrounding area as a function of the position of the optical fiber. Using the optical fiber system illustrated in Figure 1a, we can measure the bending of two optical fiber by the relationship between their difference in axial strain and curvature κ (Gander et al., 2000)

$$\kappa = \frac{\Delta\varepsilon_{mm}}{r}\,, \tag{1}$$

where $\Delta\varepsilon_{mm}$ is the difference in strain and r is the distance between two optical fibers. At least two optical fibers are needed to resolve bend measurement of one axis. We show the n-axis bending calculation for two horizontal optical fibers denoted with the superscript top and $bottom$

$$\kappa = \frac{\varepsilon_{mm}^{bottom} - \varepsilon_{mm}^{top}}{2\Delta n}\,. \tag{2}$$

We recognize that equation 2 effectively represents the centered finite-difference approximation of the transverse derivative of the axial strain

$$\kappa = \frac{\varepsilon_{mm}(n+\Delta n) - \varepsilon_{mm}(n-\Delta n)}{2\Delta n} \approx \frac{\partial \varepsilon_{mm}}{\partial n}\,. \tag{3}$$

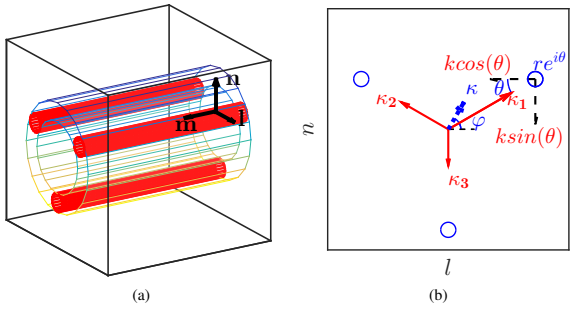

Figure 1: (a) An example of 3D parallel fiber optic configuration with local coordinates and (b) the cross section of a cable with (b) three optical fiber core (circles) with respective curvature vectors (solid line). The resultant vector (dotted line) is the sum of the respective curvature vectors.

We can generalize this idea to 3D by calculating the axial strain gradient between the optical fibers. Moore and Rogge (2012)

show that the 2-axis bend measurement calculation can be obtained with an arbitrary circular arrangement. An example of the arrangement is shown in Figure 1a. The expression needed to calculate local curvature vector for the respective optical fibers is (Moore and Rogge, 2012)

$$\boldsymbol{\kappa}_i = \frac{\varepsilon^i_{mm}}{2\Delta n}\left(cos\left(\theta_i\right)\hat{n} + sin\left(\theta_i\right)\hat{l}\right) , \tag{4}$$

where i is the optical fiber index, θ_i is the angle between the positive l-axis of the respective optical fiber as shown in Figure 1b. Expression equation 4 decomposes the scalar curvature into a vector curvature based on a local coordinate system of the cable as the reference axis. The resultant curvature vector $\boldsymbol{\kappa}$ represents the overall bending of the optical fiber by summing all the curvature vectors of the respective optical fibers

$$\boldsymbol{\kappa} = \sum_{i=1}^{N} \boldsymbol{\kappa}_i . \tag{5}$$

Calculating the angle made by $\boldsymbol{\kappa}$ with respect to the reference axis gives

$$\boldsymbol{\varphi} = tan^{-1}\left(\frac{\kappa_n}{\kappa_l}\right) , \tag{6}$$

and its derivative of the angle we can obtain the torsion of the optical fibers as

$$\tau = \frac{d\varphi}{dm} . \tag{7}$$

The curvature $\boldsymbol{\kappa}$ allow us to compute the displacement components through the geometrical definition

$$\boldsymbol{\kappa} = \frac{\partial^2 u_l}{\partial m^2}\hat{l} + \frac{\partial^2 u_n}{\partial m^2}\hat{n} . \tag{8}$$

Solving equation 8 using the calculated curvature yields the transverse displacement components (u_l and u_n). The axial displacement u_m is the integration of the measured axial strain ε_{mm} along the optical fiber. Therefore, we can obtain all the displacement components with respect to the local coordinate system of the optical fiber given that we have at least three parallel optical fibers.

Plane wave example

We consider planar P and S waves impinging at an angle on the optical fiber to illustrate the measures of axial strain. This example shows compression and elongation along the optical fiber for both wave modes which is observed through the axial strain tensor shown in Figures 2a and 2b. The axial strain for both P and S waves show that they share the same sign although they are different in terms of polarization, therefore both P and S waves share the same gradient. As the curvature measurement is ultimately the gradient of axial strain in the transverse direction, P and S waves have the same curvature to calculate the displacement u_n in the **n**-direction as shown in Figures 3c and 3d. The consequence of the similar gradient of axial strain, we are unable to reconstruct the transverse displacement component with the correct sign for S-waves as illustrated by Figure 3f where the S-wave points in the direction of P-waves.

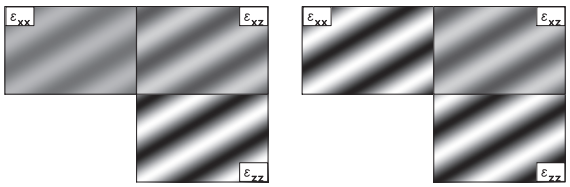

Figure 2: Strain tensor for plane (a) P-wave and (b) S-wave propagating with an incidence angle of 30°.

Discussion

Using the analytical plane waves example, we show the lack of information using the axial strain itself when we calculate the curvature for both P and S waves that are used to reconstruct the displacement components. The axial strain does not contain information to evaluate the polarization direction of different wave modes. This creates an ambiguity in reconstructing the displacement field.

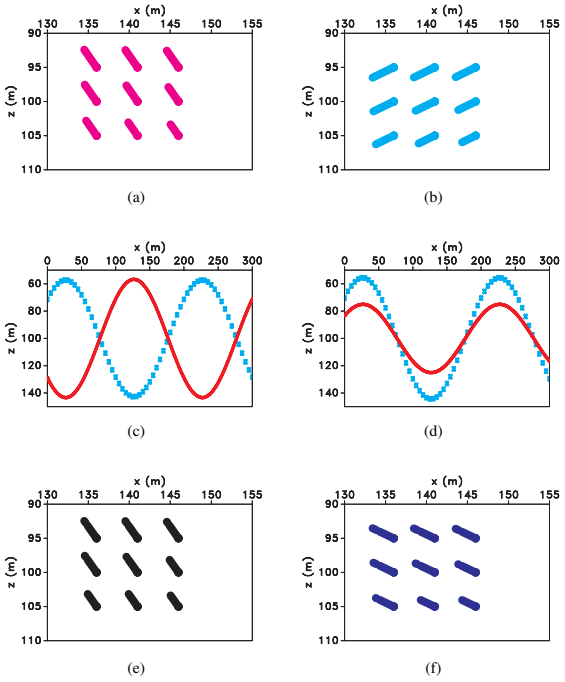

Figure 3: The control (a) P-wave (arrow pointing top right) and (b) S-wave exaggerated displacement vectors (arrow pointing bottom right). The scaled curvature (dotted line) and displacement (solid line) for (c) P-wave and (d) S-wave. The reconstructed exaggerated displacement vectors for (e) P- and (f) S-waves using the calculated curvature.

Our results show the calculated curvatures for P and S waves have the same sign as a result of the same sign for the measured axial strain. The reconstructed displacement shares the same sign as the curvature. However, the analytical displacement results for P- and S-wave do not share the same sign. The

disagreement between the curvature sign and the displacement for S-wave is not a result of an incorrect curvature calculation, but that of insufficient information to provide the reconstruct the displacement with the appropriate sign.

Based on the reconstructed displacement results, multiple parallel optical fibers do not give us enough information to accurately reconstruct the multicomponent DAS data. In the following section, we propose a different optical fiber layout that can provide adequate information, under certain assumptions, for multicomponent DAS data reconstruction.

HELICAL OPTICAL FIBER

A helical optical fiber configuration for Distributed Acoustic Sensing (DAS) (Den et al., 2013) is designed to detect broadside acoustic signals, which refers to waves that arrive perpendicular to the direction along the optical fiber. Here, we exploit the helical shape as a tool to measure different projections of the strain field along the optical fiber.

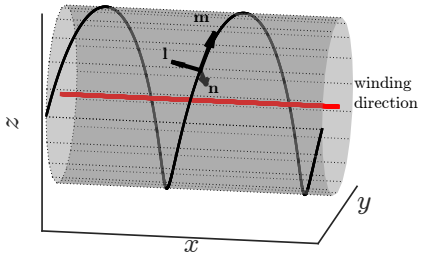

Figure 4: An example of the helical optical fiber with the associated local coordinate system.

In this configuration, we make the assumption that the wavelength of the wavefield is much greater than the spatial wavelength of the helical optical fiber. This assumption is important so that we can group multiple measurements along the optical fiber to refer to the same strain tensor field.

The relationship between the axial strain measured by the optical fiber and the strain tensor of the surrounding area via the angles can be expressed as (Young and Budynas, 2002)

$$\boldsymbol{\varepsilon}' = \mathbf{R}\boldsymbol{\varepsilon}\mathbf{R}^{\mathbf{T}}\,, \tag{9}$$

where the symbol $(\prime)$ denotes rotated strain tensor and $\mathbf{R}$ represents the rotation matrix. Rotation of a coordinate system can be written

$$\overset{\mathbf{x}'}{\begin{bmatrix} m_1 & l_1 & n_1 \\ m_2 & l_2 & n_2 \\ m_3 & l_3 & n_3 \end{bmatrix}} = \overset{\mathbf{R}}{\begin{bmatrix} R_{11} & R_{12} & R_{13} \\ R_{21} & R_{22} & R_{23} \\ R_{31} & R_{32} & R_{33} \end{bmatrix}} \overset{\mathbf{x}}{\begin{bmatrix} 1 & 0 & 0 \\ 0 & 1 & 0 \\ 0 & 0 & 1 \end{bmatrix}}\,, \tag{10}$$

where $\mathbf{x}'$ denotes axes of the rotated coordinate system and $\mathbf{x}$ represents axes of the original coordinate system which is an identity matrix. Therefore, the rotation matrix is represented by the local coordinate system of the optical fiber. Since the primary strain measurement of the optical fiber is due to axial strain only, we can narrow the problem to the rotated axial strain measurement in 3D at a location along the optical fiber as follows

$$\overset{\mathbf{d}}{\left[\varepsilon_{mm}\right]} = \overset{\mathbf{G}}{\begin{bmatrix} R_{11}^2 & R_{12}^2 & R_{13}^2 & 2R_{11}R_{12} & 2R_{11}R_{13} & 2R_{12}R_{13} \end{bmatrix}} \overset{\mathbf{m}}{\begin{bmatrix} \varepsilon_{xx} \\ \varepsilon_{yy} \\ \varepsilon_{zz} \\ \varepsilon_{xy} \\ \varepsilon_{xz} \\ \varepsilon_{yz} \end{bmatrix}}\,, \tag{11}$$

where the observed data $\mathbf{d}$ vector represents axial strain measurements along a segment of the optical fiber of length h which is assumed to be much smaller than the wavelength of the wavefield. The matrix $\mathbf{G}$ represents the expanded rotation matrix from equation 10. The number of rows in the data vector and matrix $\mathbf{G}$ refers to the number of measurements that refers to the same strain tensor of the surrounding area.

The expression in equation 11 can be solved using least-squares inversion where the kernel or forward operator $(\mathbf{G})$ is known. The data $(\mathbf{d})$ are the recorded axial strains along a segment of the helical optical fiber (this gives axial strain as a function of angles, given the assumption that the seismic wavelength is much larger than the helix period holds) and the model $(\mathbf{m})$ is the strain tensor of the surrounding area. Therefore, the model can be expressed as

$$\mathbf{m} = \left(\mathbf{G}^{\mathbf{T}}\mathbf{G}\right)^{-\mathbf{1}}\mathbf{G}^{\mathbf{T}}\mathbf{d}\,. \tag{12}$$

The number of axial strain measurements with the associated angles can be varied accordingly with the parameters of the helix such as the radius of the helix, the distance between the windings and the interval at which the measurements are made. In Figure 5f, we show an example of the number of measurable axial strain with the respectively associated angles. The example is designed with a radius and a distance between the windings which are much smaller than the wavelength of the wavefield. Using the same parameters, Figure 5e shows a 3D example with the associated angle and azimuth of the measured locations along the fiber. The 3D plot shows a constant measuring angle due to the characteristic of the helix with a constant wrapping angle thus, this configuration could not provide a range of angle dependent measurement to determine the strain tensor of the surrounding area.

By introducing a varying winding distance along the fiber, we obtain a better coverage for the measured angle dependent axial strain. This alternative configuration in 2D represents a chirp function as shown in Figure 5d. Using the chirping helix measurements, we can solve equation 12 to obtain the strain tensor of the surrounding area.

Plane wave example

Assuming that the seismic wavelength is much larger than the helix period, we are able to measure axial strain $\varepsilon_{mm}(\theta)$ as a function of angle. The strain tensors of P- and S-waves are different as shown in Figure 7a and 7b. Therefore, the measured axial strain as a function of angles for P- and S-waves are different due to the contribution of all the elements in the strain tensor as expressed in equation 11. An example of a rotated strain field at a specific time for all angles is shown in Figure 6a for P-wave and Figure 6b for S-wave that illustrates the

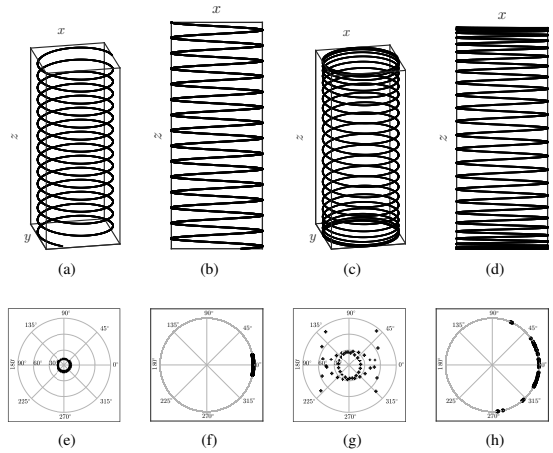

Figure 5: Example of a helical configuration for a constant wrap angle in (a) 3D and (b) 2D together with the (e) angles and azimuth for 3D and (f) angles for 2D. An example of a chirping helical configuration in (c) 3D and (d) 2D together with the (g) angles and azimuth for 3D and (h) angles for 2D.

difference between the wave modes. By using the observed rotated axial strain data and solving equation 12, we successfully reconstruct the strain field for the plane P-wave (Figure 7c) and the S-wave (Figure 7d).

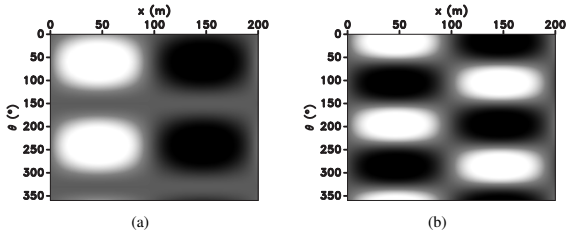

Figure 6: Axial strain of optical fiber for plane (a) P-wave and (b) S-wave with a wavelength of $100m$ as a function of angles θ at a specific time. The difference in the rotated strain field of P- and S-wave is due to the difference its respective strain tensor contributing in the projection to the axial strain of the optical fiber.

Discussion

Our synthetic example indicates that we can reconstruct the strain tensor field if we have the angle dependent axial strain measurements. As seen in Figure 5f and 5h, the chirping helix can provide a wider range of angles with respect to the winding direction of the traditional helix with a constant wrap angle. In situations where the period of the helix is equivalent to the Distributed Acoustic Sensing (DAS) system measuring distance Δh, the traditional helix can only provide a constant angle for the axial strain measurement whereas the chirping helix can provide a range of angles due to the change in the helix coil frequency.

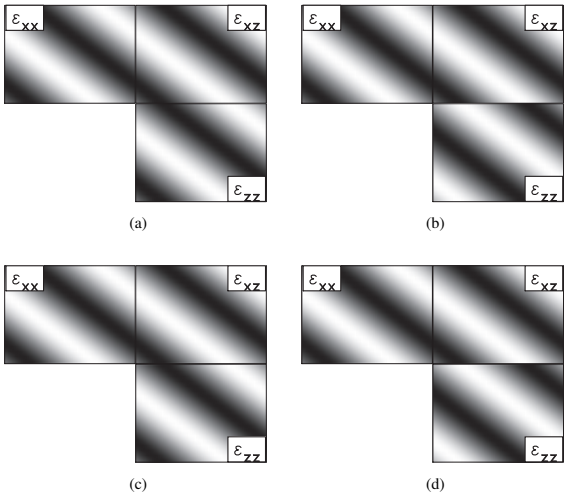

Figure 7: Strain field for plane (a) P-wave and (b) S-wave propagating at 30°. The reconstructed (c) P-wave and (d) S-wave by solving the least-squares inversion problem using the angle dependent axial strain measurements. The vertical axis is time and the horizontal axis is the receivers.

CONCLUSIONS

Multiple parallel optical fibers or a single helical optical fiber have the potential to provide multicomponent DAS data. However, the shape sensing method applied by the parallel optical fibers is unable to accurately reconstruct correct displacements when multiple wave modes are involved. The reliance of this method on the gradient of the axial strain with respect to multiple parallel optical fibers is insufficient due to lack of additional information to relate curvature to the polarization of the incident wavefields.

However, the strain tensor can be reconstructed given enough angle dependent axial strain measurement associated with a fix position along the optical fiber. This is true even for multiple wave modes as the strain tensor of the respective wave modes contributes to the axial strain along the optical fiber. The angle dependent measurement can be obtained using the helical optical fiber under the assumption that the seismic wavelength is much larger than the helix period. Alternative to the optical fiber helix shape allow us to measure a wider range of angle dependent axial strains compared to the traditional helix and can reduce the possibility of repeated angle dependent measurements.

ACKNOWLEDGMENTS

We thank the sponsors of the Center for Wave Phenomena, whose support made this research possible. The reproducible numeric examples in this paper use the Madagascar open-source software package (Fomel et al., 2013) freely available from http://www.ahay.org.

REFERENCES

Cox, B., P. Wills, D. Kiyashchenko, J. Mestayer, J. Lopez, S. Bourne, R. Lupton, G. Solano, N. Henderson, D. Hill, et al., 2012, Distributed acoustic sensing for geophysical measurement, monitoring and verification: CSEG Recorder, **37**, 7–13.

Daley, T. M., B. M. Freifeld, J. Ajo-Franklin, S. Dou, R. Pevzner, V. Shulakova, S. Kashikar, D. E. Miller, J. Goetz, J. Henninges, et al., 2013, Field testing of fiber-optic distributed acoustic sensing (DAS) for subsurface seismic monitoring: The Leading Edge, **32**, 699–706.

Den, B., A. Mateeva, J. Pearce, J. Mestayer, W. Birch, J. Lopez, K. Hornman, and B. Kuvshinov, 2013, Detecting broadside acoustic signals with a fiber optical Distributed Acoustic Sensing (DAS) assembly. (WO Patent App. PCT/US2012/069,464).

Fender, A., W. MacPherson, A. Moore, J. Barton, J. Jones, S. McCulloch, B. Jones, D. Zhao, L. Zhang, and I. Bennion, 2006, Dynamic two-axis curvature measurement using multicore fiber Bragg gratings: Optical Fiber Sensors, Optical Society of America, TuE87.

Flockhart, G., W. MacPherson, J. Barton, J. Jones, L. Zhang, and I. Bennion, 2003, Two-axis bend measurement with Bragg gratings in multicore optical fiber: Optics letters, **28**, 387–389.

Fomel, S., P. Sava, I. Vlad, Y. Liu, and V. Bashkardin, 2013, Madagascar: open-source software project for multidimensional data analysis and reproducible computational experiments: Journal of Open Research Software, **1**.

Gander, M., W. MacPherson, R. McBride, J. Jones, L. Zhang, I. Bennion, P. Blanchard, J. Burnett, and A. Greenaway, 2000, Bend measurement using Bragg gratings in multicore fibre: Electronics Letters, **36**, 1.

Lumens, P., A. Franzen, K. Hornman, S. G. Karam, G. Hemink, B. Kuvshinov, J. La Follett, B. Wyker, and P. Zwartjes, 2013, Cable development for distributed geophysical sensing with a field trial in surface seismic: Fifth European Workshop on Optical Fibre Sensors, International Society for Optics and Photonics, 879435–879435.

Lumens, P. G. E., 2014, Fibre-optic sensing for application in oil and gas wells: Technische Universiteit Eindhoven.

Madsen, K. N., M. Thompson, T. Parker, and D. Finfer, 2013, A VSP field trial using distributed acoustic sensing in a producing well in the north sea: First Break, **31**, 51–56.

Mateeva, A., J. Lopez, J. Mestayer, P. Wills, B. Cox, D. Kiyashchenko, Z. Yang, W. Berlang, R. Detomo, and S. Grandi, 2013, Distributed acoustic sensing for reservoir monitoring with VSP: The Leading Edge, **32**, 1278–1283.

Mateeva, A., J. Mestayer, B. Cox, D. Kiyashchenko, P. Wills, J. Lopez, S. Grandi, K. Hornman, P. Lumens, A. Franzen, et al., 2012, Advances in distributed acoustic sensing (DAS) for VSP: Presented at the 2012 SEG Annual Meeting, Society of Exploration Geophysicists.

Mestayer, J., B. Cox, P. Wills, D. Kiyashchenko, J. Lopez, M. Costello, S. Bourne, G. Ugueto, R. Lupton, G. Solano, et al., 2011, Field trials of distributed acoustic sensing for geophysical monitoring: Presented at the 2011 SEG Annual Meeting, Society of Exploration Geophysicists.

Moore, J. P., and M. D. Rogge, 2012, Shape sensing using multi-core fiber optic cable and parametric curve solutions: Optics express, **20**, 2967–2973.

Young, W. C., and R. G. Budynas, 2002, Roark's formulas for stress and strain: McGraw-Hill New York, **7**.